Journal of Power Sources 190 (2009) 435–446

Contents lists available at ScienceDirect

Journal of Power Sources

journal homepage: www.elsevier.com/locate/jpowsour

Lattice Boltzmann simulations of liquid droplet dynamic behavior on a hydrophobic surface of a gas flow channel

Liang Hao, Ping Cheng*

Ministry of Education Key Laboratory of Power Machinery and Engineering, School of Mechanical and Power Engineering, Shanghai Jiaotong University, Shanghai 200240, PR China

ARTICLE INFO

Article history:
Received 15 December 2008
Received in revised form 13 January 2009
Accepted 13 January 2009
Available online 21 January 2009

Keywords:
Lattice Boltzmann method
Droplet
Dynamic behavior
Gas flow channel
Detachment

ABSTRACT

Using the multiphase free-energy lattice Boltzmann method (LBM), the formation of a water droplet emerging through a micro-pore on the hydrophobic gas diffusion layer (GDL) surface in a proton exchange membrane fuel cell (PEMFC) and its subsequent movement on the GDL surface under the action of gas shear are simulated. The dynamic behavior of the water droplet emergence, growth, detachment and movement in the gas flow channel is presented. The size of the detached droplet and the time of the droplet removing out of the channel under the influence of gas flow velocity and GDL surface wettability are investigated. The results show that water droplet removal is facilitated by a high gas flow velocity on a more hydrophobic GDL surface. A highly hydrophobic surface is shown to be capable of lifting the water droplet from the GDL surface, resulting in more GDL surface available for gas reactant transport. Furthermore, an analytical model based on force balance is presented to predict the droplet detachment size, and the predicted results are in good agreement with the simulation results. It is shown that the LBM approach is an effective tool to investigate water transport phenomena in the gas flow channel of PEMFCs with surface wettability taken into consideration.

1. Introduction

Proton exchange membrane fuel cells (PEMFCs), as an attractive power source for automotive and portable applications, have been given much attention in the last decade. In a PEMFC cathode, oxygen is supplied to the gas flow channel and transfers to the catalyst layer where electrochemical reactions occur and water is produced as shown in Fig. 1(a). The transport of the produced water has a significant influence on the performance of PEMFCs [1]. In order to maintain high proton conductivity, it is necessary to keep sufficient water content in the membrane. On the other hand, too much water in the cathode can cause flooding in the porous gas diffusion layer (GDL) or clogging of the gas flow channel by the accumulated liquid water, thus resulting in the inhibition of the gaseous reaction transport to the reaction sites [2]. Therefore, water management is considered to be a critical issue on the performance of PEMFCs.

Previous studies on the water transport in the PEMFCs have mainly focused on the water distribution in the porous GDL, which has been assumed to be a homogeneous medium [3–6]. Although the clogging of the gas channel could cause severe increase of the gas flow pressure loss thus leading to more serious degradation of fuel cell performance than GDL flooding, water transport in the gas flow channel has not been given adequate attention until recently. In almost all of the numerical studies, water in the gas channel is simply assumed to be vapor flow or mist flow [7]. Visualization studies, however, did not support such an assumption. In practice, water is often accumulated to form individual droplets through pores emerging on the GDL surface [8–11], which is schematically shown in Fig. 1(a). Yang et al. [8] performed a detail optical visualization experiment on water droplet dynamics at high current densities and operating temperatures representative of automotive PEMFCs, and confirmed the appearance of water droplets in the gas flow channel. Using high-resolution images, the mechanics of liquid water emergence on the hydrophobic GDL surface, droplet growth and departure, as well as the two-phase flow in the gas flow channel, is characterized. Recently, neutrons imaging technique [9,10] and gas chromatography measurements [11], as well as pressure drop measurement [12,13] which is related to the water content in the gas flow channel, have also been used to probe water droplet formation and distribution in the gas flow channel in operating PEMFCs, and similar visualization results have been shown. These studies have provided some basic understanding of water transport in the gas flow channel but they were all limited to qualitative investigations. It has been known that the size and distribution of the water droplet, as well as the geometry of the gas channel and the wettability property of the GDL have remarkable effects on water removal. Thus, in order to obtain a thorough understanding of this issue, quantitative results are needed.

* Corresponding author. Tel.: +86 21 34206337; fax: +86 21 34206337.
E-mail address: pingcheng@sjtu.edu.cn (P. Cheng).

0378-7753/$ – see front matter © 2009 Elsevier B.V. All rights reserved.
doi:10.1016/j.jpowsour.2009.01.029

Nomenclature

A, B	free-energy parameter
Bo	bond number
b	width of the channel above the droplet
Ca	capillary number
c	lattice speed
c_s	sound speed
D	droplet diameter
d	GDL pore equivalent diameter
$\mathbf{e}$	lattice velocity vector
$\mathbf{F}$	body force vector
F_p	pressure force
F_{shear}	shear force
$F_{surface}$	surface force
f, g	distribution function
H	channel height
h	droplet height
$\mathbf{I}$	unit tensor
L	contact line length
l_0	length scale
M	mobility
$\mathbf{P}$	pressure tensor
p	pressure
Q_d	water flow rate
R	droplet radius
t_0	time scale
t_m	droplet moving time
t_f	droplet formation time
U	velocity magnitude
$\mathbf{u}$	velocity vector
V_d	detached droplet volume
w	weight coefficient
$\mathbf{x}$	position vector

Greek symbols

Γ	mobility coefficient
δt	time step
δx	lattice distance
η	dynamic viscosity
Θ	wetting potential
θ	contact angle
κ	surface tension parameter
μ	chemical potential
ξ	phase interface width
ρ	density
σ	surface tension
τ_f, τ_g	relaxation parameter
ν	kinematic viscosity
φ	order parameter
ψ	bulk free-energy density

Superscripts

a	air
ch	chemical
d	droplet
eq	equilibrium
f	fluid
hy	hydrostatic
in	inlet
k	dimension
l	lattice unit
p	physical unit
s	solid
th	thermodynamic
α	αth direction of the lattice velocity

More recently, Zhang et al. [14] analyzed the forces acting on a static water droplet on the GDL surface based on their optical observations of an operating fuel cell. The predicted detachment diameter of water droplets emerging on the GDL was compared with experimental results. Chen et al. [15] proposed a simplified model to predict the onset of water droplet instability on a GDL under the gas flow shear based on a macroscopic force balance analysis. The gas flow velocities, channel heights and contact angle hysteresis (the difference between the advancing and receding contact angles) were taken into consideration to characterize droplet instability. The droplet instability windows predicted by this model were compared with visualization experiments and 2D finite element simulations. Following Chen's work [15], Kumbur et al. [16] proposed a similar analytical model to study effects of channel geometry and GDL surface properties such as PTFE contents on water droplet instability. The contact angle hysteresis was directly introduced into their model as an empirical correlation of PTFE content from their experiment results rather than assuming a constant value. However, these works did not provide sufficient quantitative understanding of water transport on the GDL surface as they were focused on a static water droplet, which is different from the observed dynamic characteristic of water droplet growth, departure and subsequent movement. At the same time, Kimball et al. [17,18] and Benziger et al. [19] presented a different mechanism of water droplet removal in gas flow channel, where the emerging droplets holding on the GDL surface is attributed to the surface energy of the water and the GDL pore but not the interaction between the droplet and GDL surface. Additionally, water droplet dynamic behavior on solid surfaces is a fundamental fluid mechanics problem with important applications not only in fuel cells but also in many other systems such as chemical process technologies [15] as well. In spite of this, the problem has not been thorough investigated theoretically because of the difficulty associated with the contact line dynamics, which is still a pending physical problem to be dealt with to-date [20]. Several CFD studies based on volume-of-fluid (VOF) method have also been performed to simulate the water droplet dynamic behavior and distribution in a serpentine channel with an initially prescribed water volume in the channel [21,22], but the local wettability property of the GDL surface and the water emergence process were not explicitly considered. Although the effects of gas flow velocity and GDL wettability on water droplet deformation [23,24] and formation [25,26] have also been studied most recently by VOF model, the VOF method is deficient to model dynamic contact angle change, which is a critical parameter in the droplet dynamic process in the present problem. In practice, the interface topology in the VOF method is artificially reconstructed by calculating macroscopic curvature, which has little physical basis [27,28]. Usually, in order to obtain the dynamic change of the contact angle, a complicated numerical scheme must be used to track interface change continuously in the VOF method [20]. Strictly speaking, the interface between different phase and the contact line dynamics on the solid surface were based on the mesoscopic scale [29]. Thus, mesoscopic level studies are expected to investigate accurately the effect of surface wettability of the GDL on water droplet dynamic behaviors in the gas channel.

On the other hand, the lattice Boltzmann method (LBM), based on the mesoscale kinetic theory of fluids, has been developed and applied to simulate fluid flow and various transport problems in recent years. In particular, due to the kinetic nature and no need to track the phase interface explicitly, the LBM has been found to be a very effective numerical tool to simulate multiphase, multicomponent flow problems [30–32]. More recently, some works on the application of the LBM to study the transport phenomena in PEMFCs have been carried out [33–37]. For example, Fei and Hong [33] simulated the two-phase flow of methanol/CO_2 in a microchannel as a flow passage in the GDL of a micro-direct methanol fuel

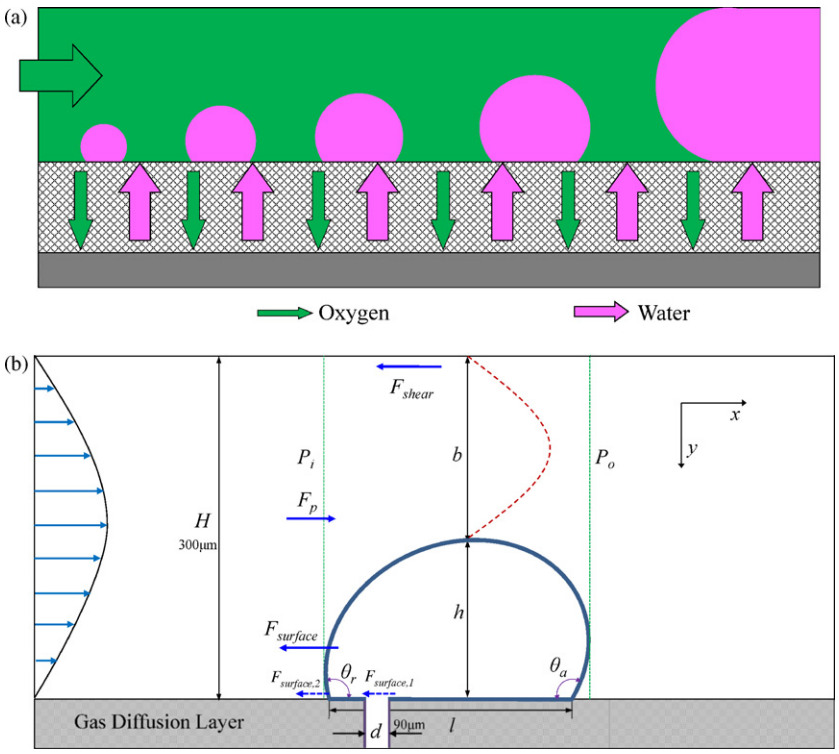

Fig. 1. (a) Schematic of the transport process in a PEMFC cathode. (b) Schematic of the force analysis of an emerging droplet.

cell, and studied CO_2 bubbly flow phenomena in the micro-channel under different operation conditions. Joshi et al. [34] used LBM to model the mass transport of H_2 and the produced H_2O (vapor) in the presence of N_2 in the 2D porous anode structure of a solid oxide fuel cell (SOFC). Suzue et al. [35] also performed a LBM simulation on multicomponent flow in a SOFC. Park and Li [36] presented a 2D two-phase LBM simulation of water droplet flowing through a fibrous structure of carbon paper GDL. Furthermore, Niu et al. [37] applied the LBM model to simulate two-phase transport in the carbon paper GDL of a PEMFC, and investigated the relative permeability under different conditions. However, the application of the LBM to study water droplet dynamics on the hydrophobic GDL surface adjacent to a gas channel has not yet been performed to-date.

In this work, the effects of gas flow velocity and GDL wettability on water droplet dynamic behavior including emergence, deformation, departure and subsequent movement in the gas flow channel with a hydrophobic GDL surface are simulated using the multiphase LBM approach based on the free-energy theory [38]. Fig. 1(a) shows a schematic of the actual water emergence process with several droplet formation spots on a GDL surface as visualized in previous experiments, and Fig. 1(b) shows its simplified version of only one water emergence pore, which will be numerically simulated in this paper. In addition, based on the forces acting on the droplet shown in Fig. 1(b), a simple analytical model is developed to predict the droplet detachment size, and comparison is made between the model predictions and the simulation results.

2. Description of the simulation model

At the present time, the intermolecular potential model and free-energy model [39] are two major approaches used in the LBM to describe multiphase systems. The former model introduces the nearest-neighboring interaction between fluid particles to describe the intermolecular potential, and the phase separation occurs with a proper potential function be chosen. However, as pointed out by He and Doolen [39], the surface tension in this model is actually a numerical artifact and its value is controlled by a force parameter, which cannot be prescribed a priori. In the latter model, the free-energy function is incorporated into the LBM to describe multiphase or multicomponent system, which has a firm theoretical basis. The surface tension as well as the contact angle when solid is present can be directly derived from the free-energy function based on Cahn–Hilliard theory [38]. Due to its more physical basis than intermolecular potential model, the free-energy LBM model has been widely used to simulate droplet formation, deformation and breakup [32,40]. Thus, this method is adopted in the present study.

2.1. LBM model

In the free-energy LBM model for two-phase system such as gas and liquid which have density of ρ_g and ρ_l, respectively, two distribution functions $f_\alpha(\mathbf{x}, t)$ and $g_\alpha(\mathbf{x}, t)$ are used to model density $\rho = \rho_g + \rho_l$, velocity $\mathbf{u}$ and order parameter φ which denotes the different phases, respectively. The evolutions of the distribution functions are described by the following equations:

$$f_\alpha(\boldsymbol{r} + \boldsymbol{e}_\alpha\delta t, t + \delta t) - f_\alpha(\boldsymbol{r}, t) = \frac{1}{\tau_f}[f_\alpha^{eq}(\boldsymbol{r} + \boldsymbol{e}_\alpha\delta t, t + \delta t) - f_\alpha(\boldsymbol{r}, t)] + F_\alpha \quad (1a)$$

$$g_\alpha(\boldsymbol{r}+\boldsymbol{e}_\alpha\delta t, t+\delta t) - g_\alpha(\boldsymbol{r}, t) = \frac{1}{\tau_g}[g_\alpha^{eq}(\boldsymbol{r}+\boldsymbol{e}_\alpha\delta t, t+\delta t) - g_\alpha(\boldsymbol{r}, t)] \quad (1b)$$

where τ_f and τ_g are two independent relaxation parameters; $\mathbf{e}_\alpha$ is lattice velocity in the αth direction and the corresponding lattice velocity directions of three-dimension 19-velocity (D3Q19) model are shown in Fig. 2. f_α^{eq} and g_α^{eq} are the equilibrium distributions of f_α and g_α, which are given as the functions of local density ρ, velocity $\mathbf{u}$ and order parameter φ, respectively:

$$f_\alpha^{eq} = A_\alpha + w_\alpha\rho\left[\frac{\boldsymbol{e}_\alpha\cdot\boldsymbol{u}}{c_s^2} + \frac{(\boldsymbol{e}_\alpha\cdot\boldsymbol{u})^2}{2c_s^4} - \frac{\boldsymbol{u}\cdot\boldsymbol{u}}{2c_s^2}\right] \quad (2a)$$

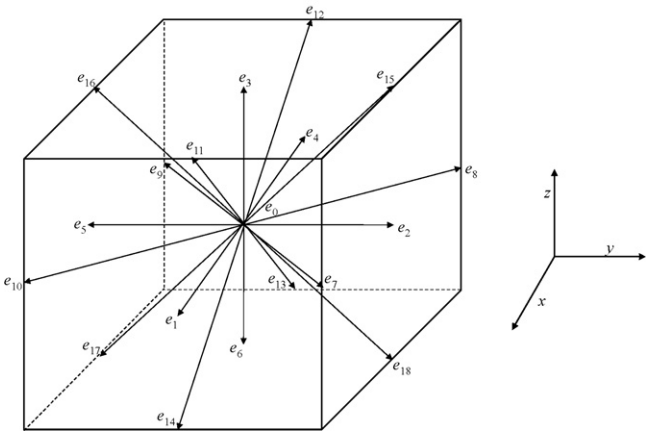

Fig. 2. Lattice velocity directions of the D3Q19 LBM.

$$g_\alpha^{eq} = H_\alpha + w_\alpha\varphi\left[\frac{\boldsymbol{e}_\alpha\cdot\boldsymbol{u}}{c_s^2} + \frac{(\boldsymbol{e}_\alpha\cdot\boldsymbol{u})^2}{2c_s^4} - \frac{\boldsymbol{u}\cdot\boldsymbol{u}}{2c_s^2}\right] \tag{2b}$$

where A_α and H_α are the indeterminate coefficients and c_s denotes the speed of sound which is given by $c/\sqrt{3}$ with $c = \delta x/\delta t$ being the lattice speed and δx being the lattice distance.

For the D3Q19 model, the lattice velocity vector $\mathbf{e}_\alpha$ and the weight coefficients w_α which depend on the lattice velocity directions are given as follows [30]:

$$\boldsymbol{e}_\alpha = \begin{Bmatrix} (0,0,0), & & & \alpha = 0; \\ (\pm1,0,0)c, & (0,\pm1,0)c, & (0,0\pm1)c, & \alpha = 1,2,\ldots,6; \\ (\pm1,\pm1,0)c, & (\pm1,0,\pm1)c, & (0,\pm1,\pm1)c, & \alpha = 7,8,\ldots,18. \end{Bmatrix}$$
$$w_\alpha = \begin{Bmatrix} 1/3, & \alpha = 0; \\ 1/18, & \alpha = 1,2,\ldots,6; \\ 1/36, & \alpha = 7,8,\ldots,18. \end{Bmatrix} \tag{3}$$

F_α in Eq. (1a) represents the body force components in lattice space, which is given by [41],

$$F_\alpha = w_\alpha\left[\frac{\boldsymbol{e}_\alpha-\boldsymbol{u}}{c_s^2} + \frac{\boldsymbol{e}_\alpha\cdot\boldsymbol{u}}{c_s^4}\boldsymbol{e}_\alpha\right]\cdot\boldsymbol{F} \tag{4}$$

with **F** the body force such as gravity.

The macroscopic local density $\rho(\mathbf{x}, t)$, momentum $\mathbf{j}(\mathbf{x}, t)$ and order parameter $\varphi(\mathbf{x}, t)$ are related to the distribution functions $f_\alpha(\mathbf{x}, t)$ and $g_\alpha(\mathbf{x}, t)$ by

$$\rho = \sum_{\alpha=0}^{18} f_\alpha; \qquad \boldsymbol{j} = \rho\boldsymbol{u} = \sum_{\alpha=0}^{18} f_\alpha\boldsymbol{e}_\alpha + \frac{\delta t}{2}\boldsymbol{F}; \qquad \varphi = \sum_{\alpha=0}^{18} g_\alpha \tag{5}$$

Since these macroscopic quantities must be locally conserved in any collision process, Eq. (5) should also be satisfied by equilibrium distribution functions f_α^{eq} and g_α^{eq}. Moreover, the resulting continuum equations from the LBM model must exactly describe the dynamics of a two-phase system [38]. Therefore, additional higher moments of f_α^{eq} and g_α^{eq} must satisfy,

$$\sum_{\alpha=0}^{18} f_\alpha^{eq}\boldsymbol{e}_\alpha\boldsymbol{e}_\alpha^{\mathrm{T}} = \boldsymbol{P}^{th} + \rho\boldsymbol{u}\boldsymbol{u}^{\mathrm{T}}; \qquad \sum_{\alpha=0}^{18} g_\alpha^{eq}\boldsymbol{e}_\alpha = \varphi\boldsymbol{u};$$
$$\sum_{\alpha=0}^{18} g_\alpha^{eq}\boldsymbol{e}_\alpha\boldsymbol{e}_\alpha^{\mathrm{T}} = \Gamma\mu\boldsymbol{I} + \varphi\boldsymbol{u}\boldsymbol{u}^{\mathrm{T}} \tag{6}$$

where $\mathbf{P}^{th}$ is the complete thermodynamic pressure tensor. Γ is the coefficient which controls the phase interface diffusion and is related to the mobility M of the fluid as follows:

$$M = \Gamma(\tau_g - 0.5)\delta t \tag{7}$$

The pressure tensor $\mathbf{P}^{th}$ and the surface tension in two-phase system, as well as the wetting boundary condition with the presence of solid wall can be determined from the free-energy basis as below.

2.2. Free-energy model

For a binary liquid system with the presence of solid boundary, the free-energy function F can be described as a function of the order parameter φ as follows [42]:

$$F = \int_V dV\left(\psi(\varphi) + \frac{\kappa}{2}(\nabla\varphi)^2\right) + \int_S dS\,\psi(\varphi_s) \tag{8}$$

where the first part on the right-hand side is the Landau free-energy function, describing equilibrium properties of the fluid system in the bulk control volume V. $\psi(\varphi)$ is the bulk free-energy density for the homogeneous system, and φ_s is the wall order parameter which is used to denote the wall wettability. The square of the gradient term denotes the free energy excess in the interfacial region, which is defined as the surface energy between different fluids with κ relating to the surface tension. The free-energy density $\psi(\varphi)$ can be chosen as the form of a double-well potential [40]:

$$\psi(\varphi) = -\frac{A}{2}\varphi^2 + \frac{B}{4}\varphi^4 \tag{9}$$

where A and B are two parameters, which are chosen by positive values for phase separation in present study. From the Landau free-energy function, the chemical potential μ is given by [40]:

$$\mu = -A\varphi + B\varphi^3 - \kappa\nabla^2\varphi \tag{10}$$

Following the Gibbs–Duhem equation, it gives:

$$\nabla\cdot\boldsymbol{P}^{ch} = \varphi\nabla\mu \tag{11}$$

with the chemical part of the thermodynamic pressure tensor $\mathbf{P}^{ch}$ given by

$$\boldsymbol{P}^{ch} = p_0\boldsymbol{I} + \kappa(\nabla\varphi)(\nabla\varphi)^{\mathrm{T}} \tag{12}$$

where **I** is the second-order unit tensor, p_0 is the scale part of the pressure tensor which can be expressed by [32,38]:

$$p_0 = \varphi u - \psi(\varphi) - \frac{\kappa}{2}(\nabla\varphi)^2 = -\frac{A}{2}\varphi^2 + \frac{3B}{4}\varphi^2 - \kappa\varphi\nabla^2\varphi - \frac{k}{2}(\nabla\varphi)^2 \tag{13}$$

The complete thermodynamic pressure tensor $\mathbf{P}^{th}$ is the sum of $\mathbf{P}^{ch}$ and the hydrostatic pressure p^{hy} as follows:

$$\boldsymbol{P}^{th} = \boldsymbol{P}^{ch} + p^{hy}\boldsymbol{I} \tag{14}$$

where p^{hy} is given by $p^{hy} = c_s^2\rho$ with c_s being the sound speed in the Lattice Boltzmann scheme. From Eqs. (12)–(14), the final bulk pressure of the binary liquid system can be obtained as

$$p = c_s^2\rho - \frac{A}{2}\varphi^2 + \frac{3B}{4}\varphi^4 - \kappa\varphi\nabla^2\varphi - \frac{k}{2}(\nabla\varphi)^2 \tag{15}$$

The minimization of the derivation of the free energy in bulk with respect to order parameter φ results in [40]:

$$\mu = -A\varphi + B\varphi^3 - \kappa\nabla^2\varphi = 0 \tag{16}$$

Thus, the equilibrium order parameter φ_0 in the bulk of the two different fluids follows $\varphi_0 = \pm(A/B)^{1/2} = \pm1$ when restricting the value $A = B$.

In addition, for a plane phase interface under equilibrium conditions, the order parameter profile across the phase interface can be represented as,

$$\varphi = \varphi_0\tanh\left(\frac{x}{\xi}\right) \tag{17}$$

where ξ is the interface width which is given by $\xi = (2\kappa/A)^{1/2}$ [32]. The interface surface tension is evaluated according to thermodynamic theory by [38],

$$\sigma = \int \kappa \left(\frac{\partial \varphi}{\partial x}\right)^2 dx \tag{18}$$

From Eqs. (17) and (18), the surface tension is obtained by,

$$\sigma = \frac{4\kappa}{3\xi}\varphi_0^2 \tag{19}$$

When specifying the surface tension σ and interface width ξ, the chemical potential μ and thermodynamic pressure tensor $\mathbf{P}^{th}$, which are used in the free-energy LBM model above, can be derived. The interface width ξ is a free parameter in this model. In order to keep a sharp phase interface, the interface width should be chosen with a small value. However, too small ξ will lead to numerical instability and inaccuracy. In this study, we specified its value as two lattice distance, which has been proved to give stable and accuracy numerical results [40].

Applying Eq. (14), the coefficients A_α and H_α in the equilibrium distribution functions given by Eqs. (2a) and (2b) can be determined from Eqs. (5) and (6) as follows:

$$A_\alpha = \begin{cases} \rho - 2(P_{xx}^{th} + P_{yy}^{th} + P_{zz}^{th})/3c^2 & \alpha = 0; \\ \boldsymbol{e}_\alpha^T \mathbf{P}^{th} \boldsymbol{e}_\alpha / 4c^4 - (P_{xx}^{th} + P_{yy}^{th} + P_{zz}^{th})/36c^2 & \alpha = 1, 2, \ldots, 6; \\ \boldsymbol{e}_\alpha^T \mathbf{P}^{th} \boldsymbol{e}_\alpha / 8c^4 - (P_{xx}^{th} + P_{yy}^{th} + P_{zz}^{th})/18c^2 & \alpha = 7, 8, \ldots, 18. \end{cases}$$

$$H_\alpha = \begin{cases} \varphi - 2\Gamma\mu/c^2 & \alpha = 0; \\ \Gamma\mu/6c^2 & \alpha = 1, 2, \ldots, 6; \\ \Gamma\mu/12c^2 & \alpha = 7, 8, \ldots, 18. \end{cases} \tag{20}$$

Employing the Chapman–Enskog multiscale analysis for D3Q19 model, the distribution evolution functions Eqs. (1a) and (1b) can lead to the Navier–Stokes equations for two-phase system [37] and an order parameter equation for phase interface evolution under the low Mach number limitation:

$$\frac{\partial \rho}{\partial t} + \nabla \cdot (\rho \boldsymbol{u}) = 0 \tag{21a}$$

$$\frac{\partial (\rho \boldsymbol{u})}{\partial t} + \nabla \cdot (\rho \boldsymbol{u}\boldsymbol{u}) = -\nabla \cdot \mathbf{P}^{th} + \nabla \cdot (\rho \nu \nabla \boldsymbol{u}) + \boldsymbol{F} \tag{21b}$$

$$\frac{\partial \varphi}{\partial t} + \nabla \cdot (\varphi \boldsymbol{u}) = M \nabla^2 \mu \tag{21c}$$

The fluid viscosity ν is related to the relaxation parameters τ_f in the LBM model by

$$\nu = \frac{(\tau_f - 0.5)\delta t}{3} \tag{22}$$

In the unequal viscosities binary liquid system, the viscosity at the phase interface can be evaluated by

$$\nu = \frac{\varphi + \varphi_0}{2\varphi_0}(\nu_l - \nu_g) + \nu_g \tag{23}$$

where ν_l and ν_g denote the viscosities of liquid and gas phases with the equilibrium order parameter of φ_0 and $-\varphi_0$, respectively. The density ρ is reflected in the order parameter φ and the real local density can be obtained in the terms of order parameter by $\rho = \rho_g + (\rho_l - \rho_g)(\varphi + \varphi_0)/2\varphi_0$ [37].

It should be noted that the surface energy between the solid wall and fluid is described by the second term in Eq. (8) with S being the wall surface area. Following the analysis in [42], if $\psi(\varphi_s)$ is expanded as a power series in the wall order parameter φ_s and keeping only the first-order term, it can be written that $\psi(\varphi_s) = \lambda\varphi_s$ with λ being a constant depending on the contact angle as will be discussed later. As a result, minimizing the free-energy function F variations at equilibrium condition results in the following expression near the wall:

$$\lambda = \kappa \frac{\partial \varphi}{\partial \vec{n}} \tag{24}$$

where $\vec{n}$ denotes the direction normal to the wall surface and pointing into the liquid. The parameter λ can further be obtained by [42]:

$$\lambda = -\Theta \sqrt{\frac{\kappa A}{2}} \tag{25}$$

with Θ being the wetting potential, which is related to the contact angle as follows:

$$\cos(\theta) = \frac{(1+\Theta)^{3/2} - (1-\Theta)^{3/2}}{2} \tag{26}$$

From Eq. (26), the wetting potential can also be obtained by equilibrium contact angle as [43]:

$$\Theta = 2\,\mathrm{sign}\left(\frac{\pi}{2} - \theta\right)\left[\cos\frac{\beta}{3}\left(1 - \cos\frac{\beta}{3}\right)\right]^{1/2} \tag{27}$$

where $\beta = \arccos(\sin^2\theta)$ and $\mathrm{sign}(\pi/2 - \theta)$ is the sign function with θ being the prescribed contact angle. In practice, when an equilibrium contact angle is prescribed, the wetting potential Θ and the parameter λ are derived from Eqs. (27) and (25), respectively. As a result, the order parameter derivative $\partial\varphi/\partial\vec{n}$ at the wall is determined from Eq. (24), which can be regarded as the wall boundary condition for order parameter φ.

3. Boundary conditions

The velocity or pressure boundary condition, which is related to the distribution function $f_\alpha(\mathbf{x}, t)$ in LBM, can be dealt with using the bounce-back of the non-equilibrium distribution rule as given by Hao and Cheng [44] for the D3Q19 model. Moreover, the order parameter boundary for the distribution function $g_\alpha(\mathbf{x}, t)$ at inlet or outlet is an additional boundary condition in the two-phase LBM compared with the single-phase model. In this study, the pure gas fluid component boundary condition is used at both the inlet and outlet of the gas channel. This boundary condition can be dealt with similar to the implementation of concentration boundary conditions for diffusion problem [45]. For example, if the inlet boundary face is assumed to be perpendicular to the x-direction with the lattice velocity e_1, e_7, e_{10}, e_{11} and e_{14} (as shown in Fig. 2) pointing into the calculation region, the distribution functions g_1, g_7, g_{10}, g_{11} and g_{14} are not determined after streaming. In order to ensure the order parameter φ_{in} at inlet equal to the prescribed value, these unknown distribution functions must satisfy,

$$g_1 + g_7 + g_{10} + g_{11} + g_{14} = \varphi_{in} - (g_0 + g_2 + g_3 + g_4 + g_5 + g_6 + g_8 + g_9 + g_{12} + g_{13} + g_{15} + g_{16} + g_{17} + g_{18}) \tag{28}$$

according to Eq. (5). Assuming that g_i ($i = 1, 7, 10, 11, 14$) are distributed by their weight coefficients w_α given in Eq. (3), it results in,

$$g_i = \frac{w_i \varphi^*}{w_1 + w_7 + w_{10} + w_{11} + w_{14}} \quad i = 1,\ 7,\ 10,\ 11,\ 14. \tag{29}$$

where φ^* is the right-hand side of Eq. (28).

In order to implement the wetting boundary condition at the solid wall of a two-phase system, the method proposed by Niu et al. [37] is adopted in the present study. In this method, the order parameter derivative in Eq. (24) is calculated by the first-difference as $\partial\varphi/\partial\vec{\boldsymbol{n}} = (\varphi_f - \varphi_s)\delta x$ with φ_s being the order parameter of the

solid and φ_f the order parameter of the fluid point adjacent to the solid wall. By substituting the differences into Eq. (24) and averaging them over the all fluid points adjacent to the solid wall, the order parameter φ_s can be approximated by

$$\varphi_s = \frac{\sum_N(\varphi_f - \delta x\lambda/\kappa)}{N} \tag{30}$$

where N is the total number of the fluid points which are nearest the solid wall. Eq. (30) can easily be applied to complex solid boundary such as porous media. As this is our first numerical simulation of droplet dynamics in gas flow channel using the free-energy method, we limited the GDL surface to be smooth in present study. This model can easily be extended to study the roughness effect of the fibrous GDL surface on droplet dynamics.

In the free-energy LBM model, the computation of derivatives $\nabla\varphi$ and $\nabla^2\varphi$ are needed to evaluate the chemical potential given by Eq. (10) and pressure tensor given by Eq. (14) as well as equilibrium distribution functions given by Eqs. (2a) and (2b). To minimize the discretization error, these derivatives are calculated using 19-point finite-difference stencils as follows [32,37]:

$$\nabla_k\varphi(\boldsymbol{r}) = \frac{\sum_{\alpha=0}^{19} w_\alpha \varphi(\boldsymbol{r} + \boldsymbol{e}_\alpha\delta t)e_{\alpha k}}{\delta t\sum_{\alpha=0}^{19} w_\alpha e_{\alpha k}^2} \tag{31a}$$

$$\nabla^2\varphi(\boldsymbol{r}) = \frac{2\sum_{\alpha=0}^{19} w_\alpha[\varphi(\boldsymbol{r} + \boldsymbol{e}_\alpha\delta t) - \varphi(\boldsymbol{r})]}{\sum_{\alpha=0}^{19} w_\alpha(e_{\alpha k}\delta t)^2} \tag{31b}$$

with $k(k = x, y, z)$ denoting the dimension.

4. Validation of the present model

To validate the present LBM model, two examples of a droplet placing in an unbounded gas domain and on a solid wall are simulated. For the first benchmark, a *two-dimensional* cylindrical liquid droplet is initially located at the center of the lattice domain with 100×100 lattices in the xy-plane. The periodic boundary conditions are imposed at all boundaries. According to the Laplace law, when the system reaches the equilibrium condition, the pressure difference between the interior and exterior of the droplet Δp is related to the surface tension σ as

$$\Delta p = \frac{\sigma}{R} \tag{32}$$

where R is the droplet radius. Fig. 3 shows the comparison of simulated pressure jump across the droplet interface versus the inverse of droplet radii with the Laplace law given by Eq. (32) for a given surface tension of 0.2. As shown, the simulation results are in excellent agreement with the Laplace law, which is represented by a solid straight line.

Next, the equilibrium contact angle of a droplet placed on the solid wall is simulated in a computational domain of $60 \times 60 \times 50$ lattices. The periodic boundaries are used in x- and y-directions while wall boundaries at top and bottom in z-direction are imposed. Initially, a water droplet of a cubic shape is located on the bottom wall, and the simulation is performed until the droplet reaches its equilibrium with an unchanged spherical-cap shape. The corresponding equilibrium contact angle of the droplet on the wall is obtained by prescribing a certain wetting potential Θ according to Eq. (26). Fig. 4(a)–(c) shows equilibrium shapes of the droplet with the wetting potential Θ being 0.3, 0 and −0.3, respectively. Their corresponding equilibrium contact angles, obtained from the interface topologies are 61°, 89° and 118°, respectively. The simulated equilibrium contact angle as a function of the wetting potential for a wider range is presented in Fig. 5, where it is shown that the simulated results by the present LBM model agree quite well with the theoretical predictions by Eq. (26) in the range of contact angle from 40° to 160° including the results presented in Fig. 4. Therefore, the present LBM model is capable of simulating two-phase flow with the presence of solid walls accurately.

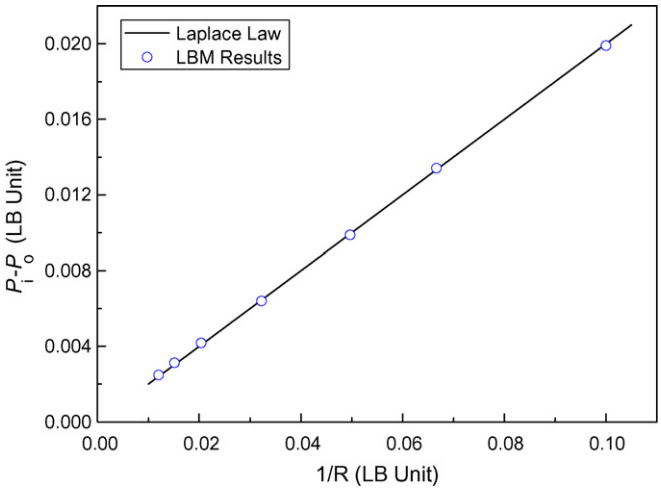

Fig. 3. Comparison of the LBM results with the Laplace law for pressure jump across a stationary droplet interface.

5. Results and discussion

5.1. Droplet formation in gas flow channel

Fig. 1(b) shows the schematic of a droplet emergence through the GDL. The computational domain includes a micro-channel with the cross section of 60 (width) × 30 (height) lattices and the length of 120 lattices, as well as a GDL of 10 lattices thickness with a single square pore locating at the midline of the channel. The side length of the micro-pore is 9 lattices and one lattice distance represents 10 μm of the physical length in present study. Thus, the micro-channel has a representative geometrical size of gas flow channel used in a micro-PEMFC [46] and the micro-emergence pore has its diameter close to the bigger pores of the carbon paper GDL [20]. This is consistent with experimental observation that water usually emerges on the GDL surface along the fixed paths including larger and less hydrophobic pores in GDL [8,17–19,47]. The contact angle of the pure PTFE material is reported to be ∼110° and the contact angle of the GDL surface treated by PTFE can reach to 170° due to roughness [19]. Therefore, the contact angle of the bottom hydrophobic GDL surface is considered to be in the range of 110–170° in this study. Additionally, since the interaction between the droplet and the sidewalls is not considered here, it is assumed that the wettability of the two sidewalls and top wall are all hydrophilic with 60° contact angle. In addition, the velocity of the water through the square pore is fixed at 0.075 m s^{-1}, which is close to the value used by Chen et al. [15]. The Reynolds number Re for gas flow is restricted to be smaller than 100 with the channel equivalent diameter (400 μm) being the characteristic length. To relate the physical space with lattice space, a length scale $l_0 = 10$ μm and a time scale $t_0 = 3.5 \times 10^{-7}$ s are chosen, which results in the physical velocity u_p rescaled to the lattice velocity u_L by $u_L = u_p t_0/l_0$. The grid effect is tested by performing additional simulations in a finer grid with $l_0 = 5$ μm. The results show similar behavior of water droplet dynamics for both two grid sizes and the difference of the formed droplet size between them is below 5%. So the grid with $l_0 = 10$ μm is acceptable in this study. The simulated results by the LBM model on dynamics of the droplet emerging and moving in the gas flow channel with

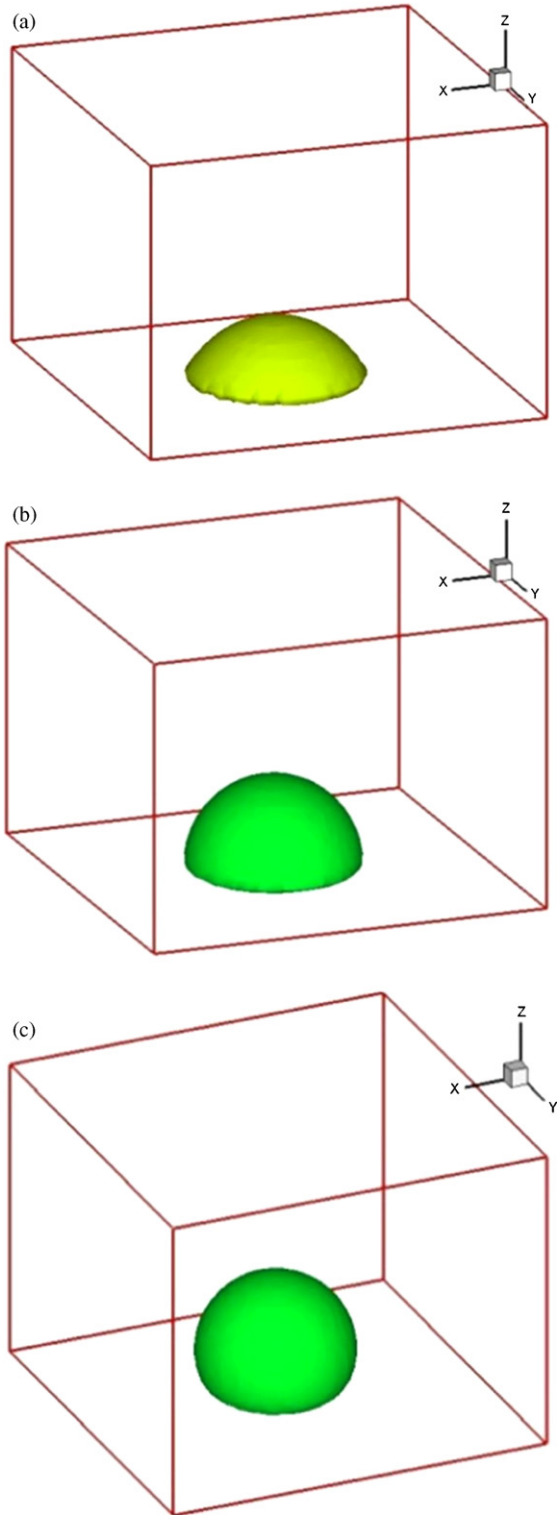

Fig. 4. Droplets on a surface with the wetting potential Θ of 0.3 (a), 0 (b) and −0.3 (c). The corresponding contact angles are 61°, 90° and 118°, respectively.

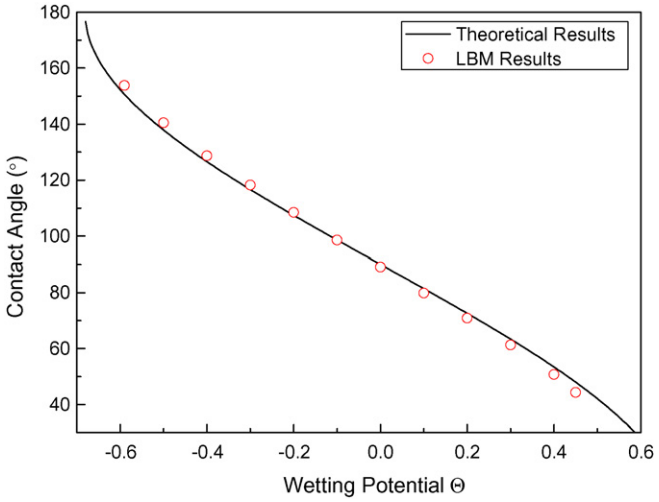

Fig. 5. Comparison of the simulated equilibrium contact angles with the theoretical predictions by Eq. (26).

various gas entering velocities and GDL wettability are presented below.

Fig. 6 shows the snapshots of droplet formation simulations for the bottom wall equilibrium contact angle of 120° and gas side capillary number Ca (defined as $Ca = \eta_a U_{in}/\sigma$, where U_{in} is the average inlet gas velocity, η_a is the gas viscosity and σ is the surface tension) of 0.06. Due to the dominate effect of surface tension, the emerging water droplet keeps an approximate spherical-cap shape above the emergence pore (see Fig. 6(a)). As the growth of the droplet, the drag force exerted on the droplet from gas shear increases and forces the droplet to creep downstream slowly (Fig. 6(b)). However, before the drag force overcomes the resistance which is dominated by the surface tension force due to the connection between the droplet and the micro-pore at this stage, the liquid water connecting bridge is maintained with the incessant emergence of water through the pore, and is elongated gradually at the same time (Fig. 6(c)), resulting in the formation of a neck after the droplet (Fig. 6(d)). Once the droplet grows larger and when the shearing stress on the droplet exceeds the surface tension force, it will accelerate and move downstream and thus the neck ruptures, inducing the final detachment of the droplet (Fig. 6(e)). Subsequently, the detached droplet moves to the outlet of the channel along the bottom wall and simultaneously a fresh droplet is formed through the micro-pore repeatedly as shown in Fig. 6(f). The simulation results in Fig. 6 capture the dynamic evolution of the droplet formation and its subsequent motion on the GDL surface, which are accordant with experimental visualizations [14]. From the above analysis, it can be concluded that the mechanism of the water droplet detachment on the assumed GDL surface can be regarded as the competition between the surface tension force from the connecting of the water in the GDL pore and the emerged part on the GDL surface, and the drag force which is related to the gas flow velocity and the droplet size in the channel. Similar conclusions were also been reported by Kimball et al. in their most recent experimental studies [17,18]. Fig. 7 shows the enlarged view of the profile of the detached droplet in Fig. 6(f) and the velocity field relative to the droplet. The deformation of the moving droplet and its rolling motion on the hydrophobic surface is clearly shown in this figure.

The effect of the GDL surface wettability on droplet dynamics can be shown by performing simulations with different equilibrium contact angles. Fig. 8 shows the droplet evolution process with bottom wall equilibrium contact angle of 165° and the capillary number of 0.06. Compared with Fig. 6 with wall equilibrium contact angle of 120°, the more hydrophobic surface causes a droplet with the larger height with the same water volume (Fig. 8(a) and (b)), thus leading to a larger drag force on it. As a result, the appearance of the neck (Fig. 8(c)) and the detachment of the droplet (Fig. 8(d)) occur earlier. However, after the detachment, the droplet seems to be lifted from the bottom surface with the contact area decreasing gradually as it moves towards to the channel

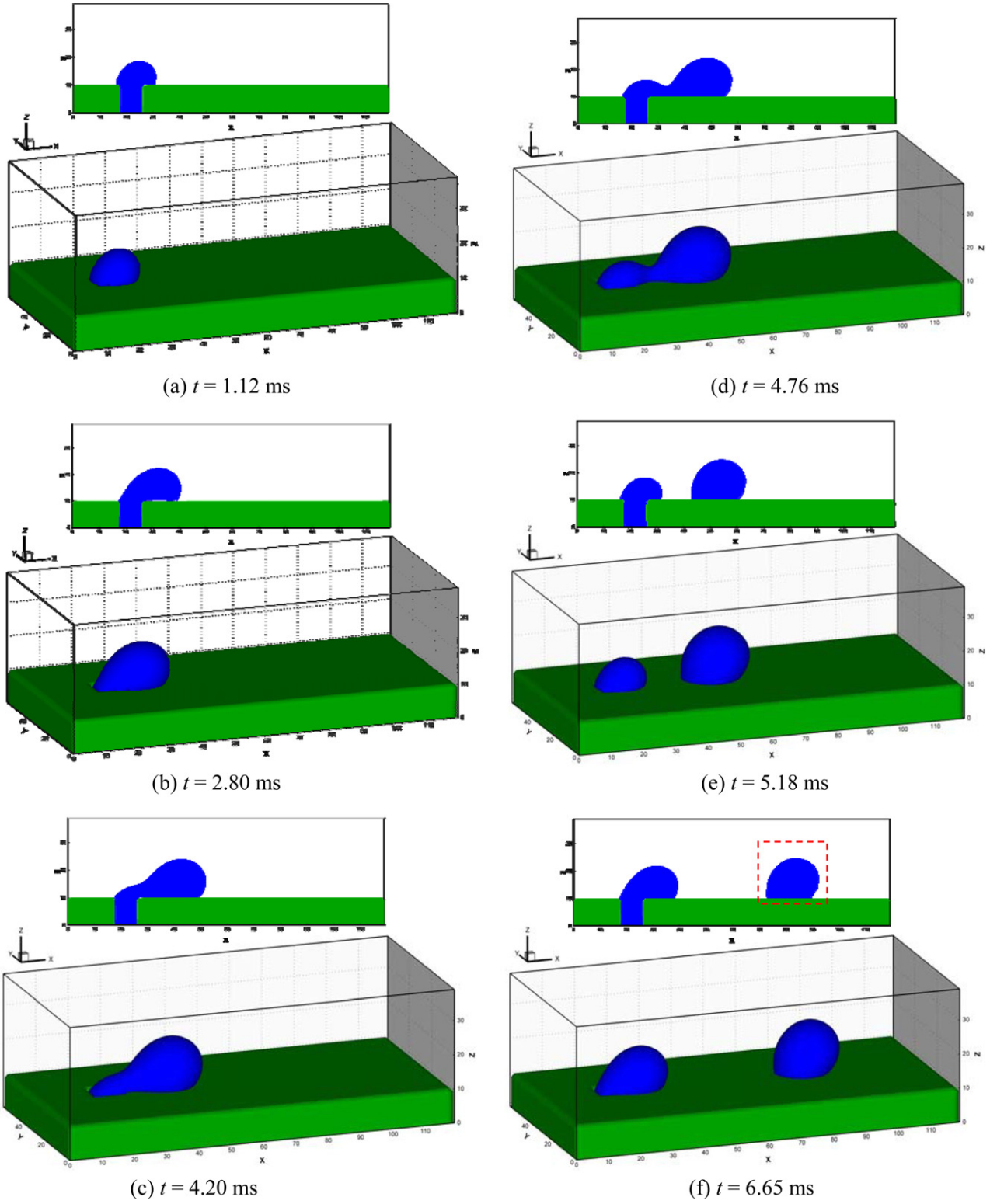

Fig. 6. Snapshots of the droplet formation (blue area denotes the droplet) through a micro-pore in the bottom wall with the equilibrium contact angle of 120° and Ca = 0.06. The upper 2D figures are the cross-sectional view on the middle section along the gas flow channel. (For interpretation of the references to color in the figure caption, the reader is referred to the web version of the article.)

outlet (Fig. 8(e)). This can be attributed to the larger lift force than adhesion force acting on the spherical droplet in the channel. In general, the adhesion force of partially wetting liquid on the solid wall is due to surface tension and this force can be approximated expressed by $F_{adhension} = 2\pi R\sigma \sin^2\theta$ for a spherical-cap droplet. If the gravity is neglected for a micro-droplet here, the droplet would lift from the surface when the lift force overcomes this adhesion force (Fig. 8(f)). The lift force is a function of the gas flow velocity [48,49] and increases with the gas flow velocity. Therefore, it can be concluded that the more hydrophobic surface and the larger gas flow velocity mean smaller adhesion force and bigger lift force, thus are beneficial for the droplet to lift from the GDL sur-

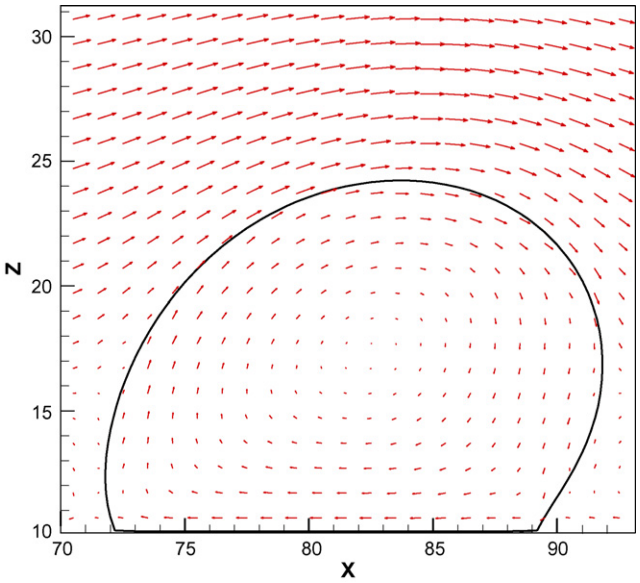

Fig. 7. Enlarged view of the profile of the moving droplet in Fig. 6(f) and the corresponding velocity field. The velocity field is relative to the droplet velocity.

face. Consequently, more GDL surface will be available for reactant transport.

The dependence of the detached droplet diameter ($D_{droplet}$) on the gas capillary number Ca and equilibrium contact angle θ is shown in Fig. 9(a) and (b), respectively. As expected, the droplet detachment size decreases with the increase of Ca and GDL hydrophobicity. However, their influence becomes weaker when Ca or θ is higher than a certain value. The simulation results of droplet dynamic behavior in gas flow channel in present study are similar to the results obtained in most recent VOF studies [23–26]. As mentioned above, the LBM model has the advantages of no need to track phase interface and the mesoscopic insight of contact angle. Thus, it is a promising method to investigate multiphase flow such as water transport in PEMFCs.

5.2. Droplet removal time

The time of the water droplet removing out of the gas flow channel is a key parameter in PEMFCs water management. It is expected that the total time of water removal is consisting of two stages, namely the formation stage and the moving stage. The formation time t_f can approximately be obtained from the flow rate Q_d of the emerging liquid water and the size of the detached droplet by $t_f = V_d/Q_d$ with V_d being the detached droplet volume, while the moving time t_m is expected to be proportional to the moving channel length, which is considered to be the distance from the emergence pore to the channel outlet (100 μm). The simulated formation time t_f and total removal time ($t_f + t_m$) of the droplet at different capillary numbers Ca and GDL equilibrium contact angles are presented in Fig. 10(a) and (b), respectively. As shown from the figures, larger Ca and GDL equilibrium contact angle result in the quicker removal of the water droplet away. However, the total removal time becomes close to the formation time gradually with the increase of the gas flow velocity (i.e., larger value of Ca), which implies that the water droplet emergence process will dominate the water droplet removal time under large gas flow velocity conditions. Moreover, the benefit of increasing hydrophobicity of GDL larger than 145° becomes unobvious for water droplet removal, as the total removal time keeps fairly flat when the equilibrium contact angle beyond 145°, although the size of the formed droplet is still decreasing. This is probably due to the lifting of the droplet from the highly hydrophobic surface, resulting in the little influence of droplet size on its moving velocity.

5.3. Analytical model on emerging droplet in micro-channel

Following the work by Chen et al. [15] as well as by Kumbur et al. [16], we now carry out a similar analysis on an emerging droplet from a micro-pore according to force balance consideration. We consider the specific case of a micro-gas flow channel with a hydrophobic GDL surface because of the usual PTFE treatment. Since surface tension plays a dominant effect on droplet behaviors in micro-channels, the capillary number is a particularly important dimensionless parameter in this study. Moreover, the Bond number Bo (defined as $Bo = \rho g D_d^2/\sigma$ with g being the gravity acceleration) is much smaller than unity in present problem, implying that the gravitational force can be neglected. Furthermore, in order to simplify the analysis, other assumptions are made as follows: (i) the gas flow in the micro-channel is fully developed laminar flow; (ii) the width of the channel is larger than its height, so that the sides of the channel have small influence on the gas flow; (iii) the droplet keeps a spherical-cap approximately with the neglecting of the deviation from the spherical shape because of the small viscous force. It should be noted that similar force analysis models have been used to investigate the liquid water droplet instability on a GDL surface [15,16,50]. In these studies, the droplet instability is controlled by the surface tension force induced by the contact angle hysteresis. However, in order to correspond to the above simulation condition for a smooth and homogenous surface, the static contact angle hysteresis of a droplet is neglected in our analytical model. Thus, the dominant surface tension force in this study is different from that in droplet instability studies.

As shown in Fig. 1(b), the control volume is denoted by the dashed line enclosing the whole droplet and the volume above it [15,16]. We choose the frame of reference with x, y-axes parallel and perpendicular to the wall, respectively. The origin of y-axis is fixed on the top wall. According to the spherical shape assumption, the droplet height h and the droplet contact diameter l on the GDL surface, as well as the gas flow width b above the droplet can be obtained from the droplet and channel geometry as follows:

$$h = R(1 - \cos\,\theta); \qquad l = 2R\sin\theta; \qquad b = H - h \tag{33}$$

where H is the channel height, R is the droplet radius and θ is the equilibrium contact angle. For a fully developed laminar flow, the gas flow profile above the droplet can be assumed to be of the Poiseuille type, which satisfies the Stokes' equation:

$$\eta_a \frac{\partial^2 u}{\partial^2 y} = \frac{dp}{dx} \tag{34}$$

where η_a denotes the gas viscosity. In addition, the moving velocity of the emerging droplet is ignored here. This assumption is approximately satisfied due to the low creeping velocity of the droplet at its growth stage and has been proved by simulations above. As a result, the solution of Eq. (34) can be obtained as

$$u = -\frac{6U_a}{b^2}y^2 + \frac{6U_a}{b}y; \qquad \frac{dp}{dx} = -2\eta_a\frac{6U_a}{b^2} \tag{35}$$

where U_a is the average gas velocity along the flow direction above the droplet and is related to the average inlet gas velocity U_{in} by

$$U_a = \frac{H}{b}U_{in} \tag{36}$$

For a Newtonian fluid, the gas shear stress at the top wall can be calculated by

$$F_{shear} = -\eta_a\frac{\partial u}{\partial y}|_{y=0}\cdot S_a = -\eta_a\frac{6U_a}{b}S_a \tag{37}$$

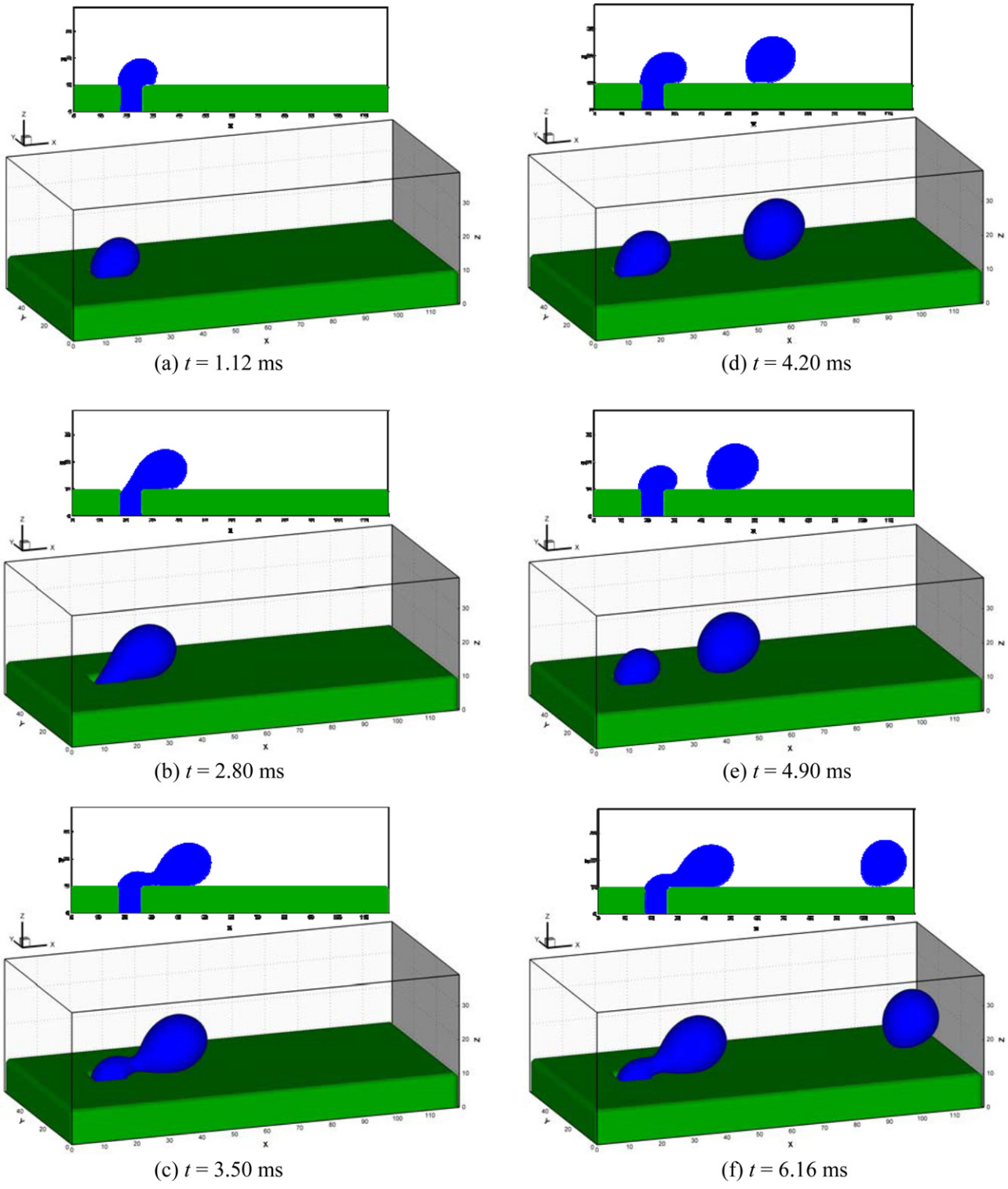

Fig. 8. Snapshots of the droplet formation (blue area denotes the droplet) through a micro-pore in the bottom wall with the equilibrium contact angle of 165° and Ca = 0.06. The upper 2D figures are the cross-sectional view on the middle section along the gas flow channel. (For interpretation of the references to color in the figure caption, the reader is referred to the web version of the article.)

where $S_a = (2R)^2$ is the contact area of the control volume on the top wall. The pressure force F_p along the flow direction is related to the pressure gradient given by Eq. (35) and the distance over the droplet by

$$F_p = (p_i - p_o)S_p = 2\eta_a \frac{6U_a}{b^2} \cdot 2RS_p \tag{38}$$

with $S_p = 2HR$ being the cross sectional area, which is perpendicular to the flow direction. Substituting Eq. (36) into Eqs. (37) and (38), the drag force acting on the droplet in the gas flow channel can be obtained from the combination of the two terms by

$$F_{drag} = \eta_a U_{in} \frac{48H^2R^2}{b^3} - \eta_a U_{in} \frac{24HR^2}{b^2} \tag{39}$$

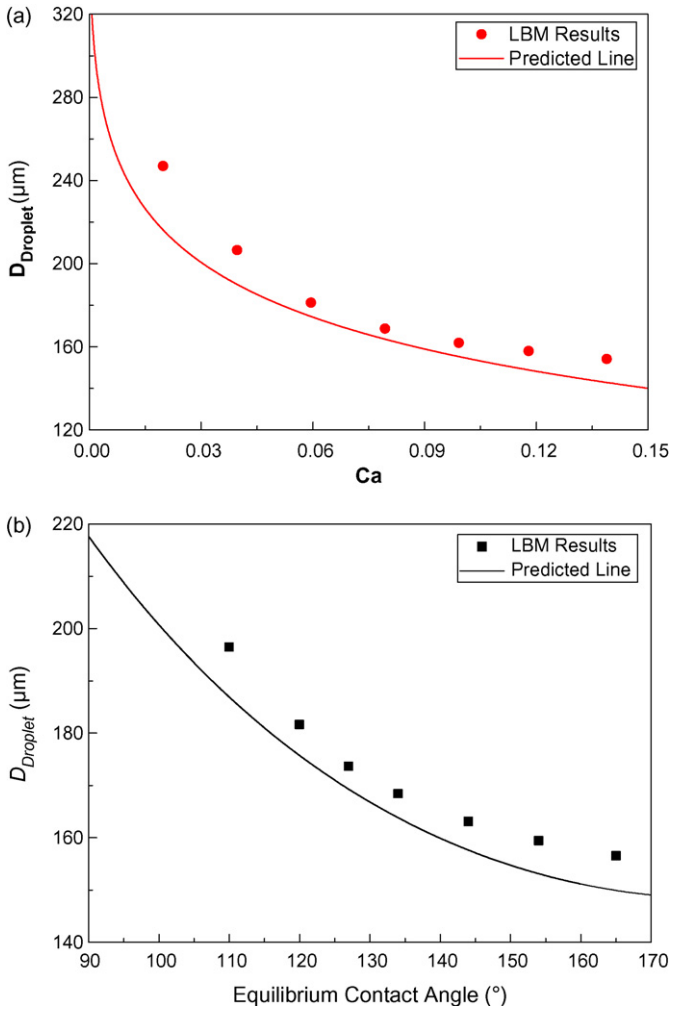

Fig. 9. (a) Comparison of the LBM simulated droplet diameters with the predictions by Eq. (42) for different capillary numbers Ca at equilibrium contact angle of 120°. (b) Comparison of the LBM simulated droplet diameters with the predictions by Eq. (42) for different equilibrium contact angles θ at $Ca = 0.06$.

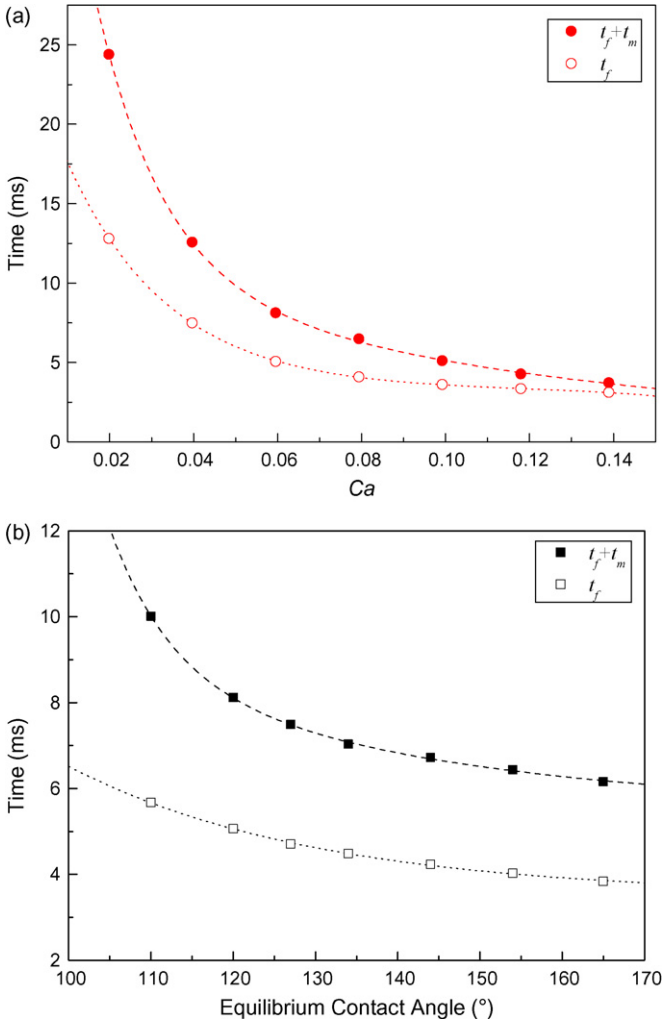

Fig. 10. (a) The simulated formation and removal time of the droplet for different capillary numbers Ca at equilibrium contact angle of 120°. (b) The simulated formation and removal time of the droplet for different equilibrium contact angles θ at $Ca = 0.06$.

Besides, the resistance force $F_{surface}$ is directly related to the surface tension and can further be divided into two terms: the surface tension force due to the connecting of the droplet to the emergence pore, and the surface tension force due to the droplet deformation. The first term is related to the size of the emergence pore as

$$F_{surface,1} = -\sigma\pi d \tag{40a}$$

with d being the equivalent diameter of the emergence pore and σ the surface tension of the liquid/gas interface. It should be noted that this surface tension force term was not considered in previous investigations on stable characteristic of a static droplet [15,16], although it has significant influence on the droplet dynamics and formation [20] and has been proved to be the dominant cohesive force for the detachment of the emerged droplet by experiments [18]. The second term of resistance force is related to the difference between the advancing and receding contact angles. If the contact line on the wall is assumed to be a circle and its semicircle at the front or rear part of the contact line is assumed to be constant advancing or receding contact angle, respectively, this resistance force is given by [51]:

$$F_{surface,2} = -\sigma(\cos\ \theta_r - \cos\theta_a)L \tag{40b}$$

where θ_r and θ_a are the receding contact angle and the advancing contact angle as shown in Fig. 1(b), and L is the contact line length of the front or rear semicircle part, given by $L = \pi l/2$. For a rough surface with a non-moving droplet, the term Eq. (40b) is related to the contact angle hysteresis, which is a function of surface properties such as roughness. However, for a smooth surface with contact line motion, it is related to the dynamic contact angle, which has been shown to be a function of the dynamic contact line velocity [52–55].

Finally, the force balance along the x-direction on the control volume, which includes an emerging droplet, results in:

$$F_p + F_{shear} + F_{surface} = 0 \tag{41}$$

Therefore, Eq. (41) provides a critical criterion for the formed droplet detaching from the emerging micro-pore. Additionally, due to the much smaller value of the droplet creeping velocity than the gas flow velocity, the force $F_{surface,2}$ deriving from droplet motion is regarded to be much smaller than $F_{surface,1}$, thus can be ignored here. As a result, substituting Eqs. (37), (38) and (40a) into Eq. (41), the force balance of an emerging droplet can further be reduced to:

$$48\frac{H^2R^2}{b^3} - 24\frac{HR^2}{b^2} = \frac{\pi d}{Ca} \tag{42}$$

So, if Eq. (33) is substituted into Eq. (42), the size of the detached droplet can be predicted in a given channel. The corresponding prediction results of the droplet size as a function of *Ca* and equilibrium contact angle θ are also plotted in Fig. 9(a) and (b) by a solid line, respectively. As shown, the predicted values are slightly smaller than the simulation results. This underestimation of droplet size can be attributed to the neglect of droplet creeping velocity in the analytical model, resulting in the underestimation of resistance force. However, theoretical prediction of this force given by Eq. (40b) has some difficulties because of the unclear physical mechanism of dynamic contact angle with contact line motion. Fortunately, the LBM model is capable of simulating the change of the dynamic contact angle at mesoscopic level, thus provides more accurate results in this study.

6. Concluding remarks

In this work, the dynamic behavior of water droplet formation and removal in the micro-gas flow channel of a PEMFC has been simulated using the multiphase free-energy LBM approach. The evolution process of water emerging through a micro-pore is clearly captured by simulation and is shown in good agreement with visualization results. The size of the detached droplet and the time of the liquid water removing out of the channel are investigated with various gas flow velocity and GDL surface wettability. The results show that the increase of the gas flow velocity and the enhancement of the GDL hydrophobicity can facilitate the formation of smaller droplets, thus decreasing the time of water droplets adhering to the GDL surface near the emergence pore. In addition, the highly hydrophobic surface is shown to promote droplet lifting from the surface after its detachment, resulting in larger GDL surface available for gas reactant transport. An analytical model is also presented to predict the droplet departure sizes based on a force balance consideration, and results from this analysis are in good agreement with that from LBM simulation under various conditions.

The results of the present study provide a mesoscopic insight for understanding the water droplet dynamic behavior in the gas flow channel of PEMFCs, which is helpful for solving the channel flooding problem. However, it should be noted that the static contact angle hysteresis, a typical characteristic of an actual roughness surface such as GDL surface, is not considered in this work. Therefore, further studies on this aspect of the problem are needed.

Acknowledgements

This work was supported by the National Natural Science Foundation of China through Grant No. 50536010 and by Nissan Company.

References

[1] C.Y. Wang, in: W. Lietsich, A. Lamm, H.A. Gasteiger (Eds.), Handbook of Fuel Cells: Fundamentals, Technology and Applications, vol. 3, part 3, John Wiley & Sons, Chichester, 2003.
[2] K. Tüber, D. Pócza, C. Hebling, J. Power Sources 124 (2003) 403–414.
[3] Z.H. Wang, C.Y. Wang, K.S. Chen, J. Power Sources 94 (2001) 40–50.
[4] L. You, H. Liu, Int. J. Heat Mass Transf. 45 (2002) 2277–2287.
[5] U. Pasaogullari, C.Y. Wang, J. Electrochem. Soc. 151 (2004) A399–A406.
[6] N.P. Siegel, M.W. Ellis, D.J. Nelson, et al., J. Power Sources 128 (2004) 173–184.
[7] C.Y. Wang, Chem. Rev. 104 (2004) 4727–4766.
[8] X.G. Yang, F.Y. Zhang, A.L. Lubawy, C.Y. Wang, Electrochem. Solid-State Lett. 7 (2004) A408–A411.
[9] R. Satija, D.L. Jacobson, M. Arif, S.A. Werner, J. Power Sources 129 (2003) 238–245.
[10] D. Kramer, J. Zhang, R. Shimoi, et al., Electrochim. Acta 50 (2005) 2603–2614.
[11] M.M. Mench, Q.L. Dong, C.Y. Wang, J. Power Sources 124 (2003) 90–98.
[12] J. St-Pierre, J. Electrochem. Soc. 154 (2007) B724–B731.
[13] X. Liu, H. Guo, F. Ye, C.F. Ma, Electrochim. Acta 52 (2007) 3607–3614.
[14] F.Y. Zhang, X.G. Yang, C.Y. Wang, J. Electrochem. Soc. 153 (2006) A225–A232.
[15] K.S. Chen, M.A. Hickner, D.R. Noble, Int. J. Energy Res. 29 (2005) 1113–1132.
[16] E.C. Kumbur, K.V. Sharp, M.M. Mench, J. Power Sources 161 (2006) 333–345.
[17] E. Kimball, T. Whitaker, I.G. Kevrekidis, J.B. Benziger, ECS Trans. 11 (2007) 725–736.
[18] E. Kimball, T. Whitaker, I.G. Kevrekidis, J.B. Benziger, AIChE J. 54 (2008) 1313–1332.
[19] J. Benziger, J. Nehlsen, D. Blackwell, T. Brennan, J. Itescu, J. Membr. Sci. 261 (2005) 98–106.
[20] A. Theodorakakos, T. Ous, M. Gavaises, et al., J. Colloid Interface Sci. 300 (2006) 673–687.
[21] P. Quan, B. Zhou, A. Sobiesiak, Z.S. Liu, J. Power Sources 152 (2005) 131–145.
[22] K. Jiao, B. Zhou, P. Quan, J. Power Sources 154 (2006) 124–137.
[23] E. Shirani, S. Masoomi, J. Fuel Cell Sci. Technol. 5 (2008) 041008.
[24] A. Golpaygan, N. Ashgriz, Int. J. Comput. Fluid Dyn. 22 (2008) 85–95.
[25] X. Zhu, P.C. Sui, N. Djilali, J. Power Sources 181 (2008) 101–115.
[26] X. Zhu, P.C. Sui, N. Djilali, Microfluid Nanofluid 4 (2008) 4543–4555.
[27] R.G.M. van der Sman, S. van der Graaf, Rheol. Acta 46 (2006) 3–11.
[28] D. Jacpmin, J. Comput. Phys. 155 (1999) 96–127.
[29] H.Y. Chen, D. Jasnow, Phys. Rev. Lett. 85 (2000) 1686–1689.
[30] P. Yuan, L. Schaefer, Phys. Fluids 18 (2006) 042101.
[31] C.U. Hatiboglu, T. Babadagli, Phys. Rev. E 76 (2007) 066309.
[32] S. van der Graaf, T. Nisisako, C.G.P.H. Schroën, et al., Langmuir 22 (2006) 4144–4152.
[33] K. Fei, C.W. Hong, Microfluid Nanofluid 3 (2007) 77–88.
[34] A.S. Joshi, K.N. Grew, A.A. Peracchio, W.S. Chiu, J. Power Sources 164 (2007) 631–638.
[35] Y. Suzue, N. Shikazono, N. Kasagi, J. Power Sources 184 (2008) 52–59.
[36] J. Park, X. Li, J. Power Sources 178 (2008) 248–257.
[37] X.D. Niu, T. Munekata, S.A. Hyodo, K. Suga, J. Power Sources 172 (2007) 542–552.
[38] M.R. Swift, E. Orlandini, W.R. Osborn, J.M. Yeomans, Phys. Rev. E 54 (1996) 5041–5052.
[39] X.Y. He, G.D. Doolen, J. Stat. Phys. 107 (2002) 309–327.
[40] G.G.M. van der Sman, S. van der Graaf, Comput. Phys. Commun. 178 (2008) 492–504.
[41] Z. Guo, C. Zheng, B. Shi, Phys. Rev. E 65 (2002) 046308.
[42] A.J. Briant, P. Papatzacos, J.M. Yeomans, Philos. Trans. R. Soc. Lond. A 360 (2002) 485–495.
[43] A.J. Briant, J.M. Yeomans, Phys. Rev. E 69 (2004) 031603.
[44] L. Hao, P. Cheng, J. Power Sources 186 (2009) 104–114.
[45] M. Yoshino, T. Inamuro, Int. J. Num. Methods Fluids 43 (2003) 183–198.
[46] J. Yu, P. Cheng, Z. Ma, B. Yi, Electrochim. Acta 48 (2003) 1537–1541.
[47] S. Litster, D. Sinton, N. Djilali, J. Power Sources 154 (2006) 95–105.
[48] J.H. Xu, G.S. Luo, G.G. Chen, J.D. Wang, J. Membr. Sci. 266 (2005) 121–131.
[49] T. Hibiki, M. Ishii, Chem. Eng. Sci. 62 (2007) 6457–6474.
[50] T. Ha, B.Y. Kim, H.S. Kim, K. Min, J. Mech. Sci. Technol. 22 (2008) 1030–1036.
[51] S. Basu, K. Nandakumar, J.H. Masliyah, J. Colloid Interface Sci. 190 (1997) 253–257.
[52] M.L. Kokko, D.H. Rothman, Phys. Rev. Lett. 98 (2007) 254503.
[53] T.D. Blake, Y.D. Shikhmurzaev, J. Colloid Interface Sci. 253 (2002) 196–202.
[54] R.G. Cox, J. Fluid Mech. 168 (1986) 169–194.
[55] P. Sheng, M.Y. Zhou, Phys. Rev. A 45 (1992) 5694–5708.